


Time-Evolved X-ray Irradiation during the 1999–2000 Outburst of the Black-Hole Binary XTE J1859+226

Mariko Kimura,¹  Chris Done²

¹*Department of Astronomy, Graduate School of Science, Kyoto University, Oiwakecho, Kitashirakawa, Sakyo-ku, Kyoto 606-8502, Japan*

²*Department of Physics, University of Durham, South Road, Durham, DH1 3LE, UK*

Accepted XXX. Received YYY; in original form ZZZ

ABSTRACT

X-ray irradiation heating of the outer disc in X-ray binaries is thought to control the decay from outburst maximum in transient systems. It is generally parameterized phenomenologically, yet here we show that it can be understood from first principles using theoretical models of irradiated discs and their coronae/winds. We test these models using five simultaneous *Hubble Space Telescope* (*HST*) and *Rossi X-Ray Timing Explorer* (*RXTE*) datasets from the black hole binary XTE J1859+226 to trace the efficiency of optical reprocessing during outburst as the source varies from the very high/intermediate state at $\sim 0.4L_{\text{Edd}}$ down through the high/soft state towards the transition to the hard state at $\sim 0.02L_{\text{Edd}}$. The models are able to predict the small change in reprocessing efficiency as the source flux decreases by a factor of two, and the spectrum softens from the very high/intermediate state to the bright high/soft state. However, the low luminosity high/soft state as well as the transition spectrum show more complex behaviour that is not well described by current models. We suggest the disc geometry has changed drastically during the outburst, probably due to tidal forces, and that the disc is no longer in steady state at the late stage of the outburst.

Key words: accretion, accretion disc – black holes physics – binaries: general – X-ray: stars – stars: individual (XTE J1859+226)

1 INTRODUCTION

Low-mass X-ray binaries (LMXBs) have a black hole or a neutron star as a central object with a companion low mass star which fills its Roche lobe. Mass transfer takes place, forming an accretion disc around the central object, and this disc is globally unstable if it crosses the Hydrogen ionisation temperature at any radius. The disc then cycles between long quiescent intervals punctuated by dramatic outbursts, with fast rise and exponential decay, during which most of the disc material is accreted (e.g., Tanaka & Shibazaki 1996; Chen et al. 1997). This is rather different to the classic disc instability mechanism as first outlined to describe normal dwarf-nova-type outbursts, which show rapid decline (Osaki 1996, for a review). In this kind of outbursts, the H-ionisation triggers a heating wave which sweeps across the disc, but the outer disc soon dips below the H-ionisation temperature, triggering a cooling wave which switches the disc back to quiescence. The major difference in behaviour between LMXBs and dwarf novae is that the central accretion flow is much brighter due to the higher gravitational

potential of the central object. X-ray irradiation from the inner disc heats the outer disc, preventing Hydrogen recombination launching a cooling wave which switches off the outburst. Such irradiation controlled decays are believed to generally match well to the observed light curves in LMXBs (Mineshige & Wheeler 1989; King & Ritter 1998; King 1998; Dubus et al. 2001; Lasota 2001; Coriat et al. 2012).

X-ray irradiation by the central bright accretion flow is then predicted to control the temperature of the outer disc. This is observable, producing reprocessed optical emission which dominates over the intrinsic dissipation (van Paradijs & McClintock 1994; de Jong et al. 1996). This X-ray heating also produces a hot disc atmosphere/wind due to another ionisation instability which operates for material in pressure balance (here, hydrostatic equilibrium). X-rays heat the surface, so it expands, and its density decreases, and its ionisation state increases so that it can be almost completely ionised. Deeper down, the material must have larger pressure in order to support the weight of the upper layers, and then, its density must increase. Bremsstrahlung cooling becomes more important, reducing the temperature, hence increasing the density to re-

* E-mail: mkimura@kusastro.kyoto-u.ac.jp

main in pressure balance. This decreases the ionisation state so that bound transitions can exist, and line cooling dramatically decreases the temperature. This leads to a sharp transition between a highly ionised atmosphere, heated to the Compton temperature, and a much more neutral disc photosphere (Krolik & Kallman 1982). The sound speed c_s of the heated atmosphere gives a typical height of $H \sim c_s/v_\phi(R)$, where v_ϕ is the Keplerian velocity of the disc, and produces a wind where $c_s > v_{\text{esc}}(R) \sim v_\phi(R)$ (Begelman et al. 1983; Woods et al. 1996; Done et al. 2018).

Hence the signatures of an irradiated outer disc are a highly ionised X-ray atmosphere/wind, reprocessed optical emission, and long decays of outbursts. However, there is as yet no detailed modelling of these effects and their observational tests. For example, the best calculations of disk-instability model first used the standard (unilluminated) disc models. These predicted that the outer regions of the disc are self-shielded (Dubus et al. 1999), so they remain unilluminated, and do not produce the observed long decays. The best irradiated disk-instability models still use an *ad hoc* illumination parameter, such that the irradiation flux $F_{\text{irr}} = CL_X/(4\pi R^2)$ (Lasota 2001; Dubus et al. 2001). The reprocessed optical emission from this can fit broadband optical/UV photometry of LMXBs (e.g., Gierliński et al. 2009), but gives a slightly different dependence than predicted by Cunningham (1976), who approximates the disc as isothermal and derive the well known scale height $H \propto R^{9/7}$ relation which leads to $F_{\text{irr}} \propto L_X/R^{12/7}$ (Hynes et al. 2002; Hynes 2005; Shidatsu et al. 2016).

In addition, as is clear from the discussion above, the disc atmosphere is in no sense isothermal, and its scale height should vary as the illuminating spectrum changes. This effect can be very large as the outburst shows a dramatic spectral transition in a way which is now well studied (Fender et al. 2004; Remillard & McClintock 2006). The spectrum starts off hard, dominated by Comptonisation, typically peaking at $2(L/L_{\text{Edd}})^{1/4}$ keV (Done et al. 2007), before making a transition back to the hard state at around $L/L_{\text{Edd}} \sim 0.02$ (Maccarone 2003). Since this changing spectrum gives a very different heating/cooling balance, the wind/atmosphere responds by changing its density/scale height/launch radius (Done et al. 2018). This means the strength of illumination should change during the outburst, but especially at the spectral transition.

We therefore address the extent of these complexities produced by X-ray irradiation via modeling the multi-wavelength spectra in one normal black-hole binary. We use the recently developed self-consistent model covering a wide energy range from hard-Xray to IR regime (Shidatsu et al. 2016). Our study enables us for the first time to find significant time variations in reprocessed fraction during outburst, to calculate how the X-ray scattered fraction should change, and to compare the observations and the predictions of reprocessing from scattering in the corona/wind. This is important for considering input values into the irradiated disc codes in order to predict the effect of X-ray illumination from a physical rather than phenomenological model, and for examining existing theories of disc instability including irradiation effect. Thus our investigations open the way to a

better understanding of the role of X-ray irradiation in the time-varying broadband spectra and light curves of LMXBs.

The amount of irradiation in the existing theories can only be well constrained with simultaneous multi-wavelength optical/UV and X-ray data. In this study, we use the unique coverage obtained from five simultaneous *HST* and *RXTE* spectra of the low galactic column black-hole binary XTE J1859+226 during its 1999–2000 outburst (Hynes et al. 2002). Although previous works used photometric optical/UV data (e.g., Gierliński et al. 2009), spectroscopic data gives a much better determination of the continuum shape, which requires *HST* in order to get the spectrum extending into the UV regime. There are very few binaries for which such data exist, especially as these are often highly reddened due to their galactic plane location, and one of them is XTE J1859+226. This object is regarded as one of normal black-hole LMXBs in terms of the overall X-ray spectral behavior and light variations (e.g., Pei et al. 2017; Nandi et al. 2018). Its multi-wavelength spectra spanning the brightest high/soft states of the outburst went through the disc dominated state on the decline and finally approached the transition to the low/hard state. Thus all these datasets should be dominated by irradiated disc emission, whereas dim low/hard states can have additional contributions from cyclo-synchrotron emission from the hot electrons (Veledina et al. 2011) and synchrotron emission from the jet, which is more likely to be an IR component (Gandhi et al. 2011; Merloni et al. 2000; Fender et al. 2004). These disc dominated states are the simpler ones in which to explore the effect of reprocessing, and were fit to the optical/UV data by Hynes et al. (2002). However, these models were not able to simultaneously reproduce the X-ray spectra. Hence, there is no study explaining coherently the broadband spectral characteristics, though there are multiple observations (Brocksopp et al. 2002; Zurita et al. 2002; Uemura et al. 2004; Casella et al. 2004; Farinelli et al. 2013; Sriram et al. 2013).

The structure of this paper is the following. In Sec. 2, we display the overall X-ray and optical behaviour of the 1999–2000 outburst in XTE J1859+226, and in Sec. 3, we describe the data selection. In Sec. 4, the details of our model are given, and the results of broadband spectral energy distributions (SED) analyses are shown in Sec. 5 and 6. Finally, we interpret and discuss our results in Sec. 7, including the results of theoretical models, and summarise our conclusions in Sec. 8.

2 OVERALL X-RAY AND OPTICAL BEHAVIOR

We use the *RXTE*/ASM standard products to look at the overall evolution of the X-ray light curve during the outburst (see the top panel in Figure 1). The corresponding ASM hardness ratios, defined as 3–12 keV/1.5–3 keV (bands 2+3/band 1), are shown in the middle panel of Figure 1. These show that the spectrum starts in the low/hard state (ASM hardness ratio around 2), then makes a transition to a softer state during the fast rise. Around the maximum, the X-ray brightness shows complex flaring (see also Brocksopp et al. 2002), and afterwards, it drops with an

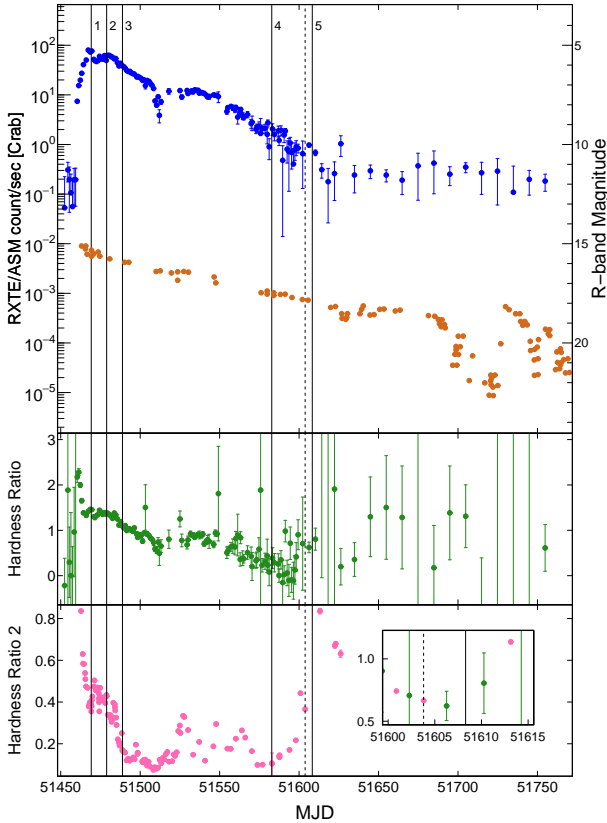


Figure 1. Overall X-ray light curve in the 1.5–12 keV band obtained by *RXTE*/ASM and overall optical *R*-band light curve digitized from Figure 2 in Zurita et al. (2002) during the 1999–2000 outburst in XTE J1859+226 (top panel), hardness ratio defined as 3–12 keV/1.5–3 keV in the *RXTE*/ASM data (middle panel), and hardness ratio calculated defined as 6–10 keV/3–6 keV in the *RXTE*/PCA data (bottom panel). The vertical solid lines labeled by 1, 2, 3, 4, and 5 represent MJD 51469, 51478, 51488, 51582, and 51608, respectively. The vertical dashed line shows February 29th in 2000 (MJD 51603). The data during MJD 51600–51680 are binned every 4 days, and those after MJD 51680 are binned every 10 days. The small window in the bottom panel shows an enlarged view of the hardness ratios during MJD 51600–51615. Here, 0.3 is added to the hardness ratios of *RXTE*/PCA data.

exponential decay with correlated spectral softening, interrupted by a plateau during MJD 51520–51545.

The *HST* data were taken on October 18th in 1999, October 27th in 1999, November 6th in 1999, February 8th in 2000, and March 5th in 2000, which correspond to MJD 51469, 51478, 51488, 51582, and 51608, respectively. These times are indicated in Figure 1 with vertical solid lines. Hereafter these are referred to as T1, T2, T3, T4, and T5. The UV and optical spectra of *HST* were taken by the Space Telescope Imaging Spectrograph (STIS), and reduced by the standard pipeline. The gratings used were G140L and G230L on the far-ultraviolet Multi-Anode Micro-channel Array (MAMA) detector, and G430L and G750L on the optical CCD. We put these in contexts of the optical evolution in the outburst by extracting the *R*-band data from Figure 2 in Zurita et al. (2002) (orange points in the upper panel of Figure 1). These show a smooth decline from T1 to T5.

The *RXTE*/PCA pointed observations give much bet-

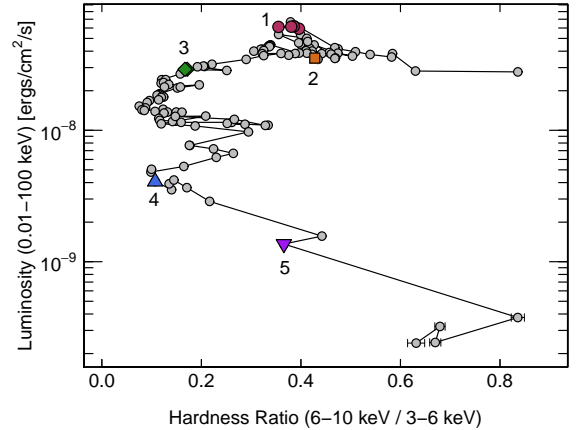


Figure 2. Hardness-intensity diagram during the 1999–2000 outburst in XTE J1859+226. The filled circles, square, diamonds, triangle, inverted triangle represent the data on MJD 51469, 51478, 51488, 51582, and 51603, respectively.

ter spectra than the ASM, but they do not give continuous coverage of the outburst. We extract the 3–25 keV standard product spectra, and fit these in XSPEC with a model consisting of $\text{Tbabs}*(\text{diskbb}+\text{nthComp})$ or $\text{Tbabs}*\text{smedge}*(\text{diskbb}+\text{nthComp}+\text{gaussian})$, with hydrogen column fixed at $5.0 \times 10^{21} \text{ cm}^{-2}$. In this paper, we use XSPEC of HEASOFT version 6.23. We use these models to calculate the intrinsic hardness ratio (unabsorbed flux in 6–10 keV/3–6 keV), shown in the bottom panel of Figure 1. This shows that there are quasi-simultaneous *RXTE*/PCA data for T1–4, but that T5 occurs during a gap in the PCA data coverage. Importantly, this gap encompasses a state change in the X-ray spectrum. The nearest PCA data taken before the *HST* spectrum is in the soft state (PCA hardness ratio ~ 0.4), while the one after is in the hard state (PCA hardness ratio ~ 0.8). The inset in the bottom panel of Figure 1 shows a zoom of this time period, with both the ASM hardness ratio (green) and the PCA hardness ratio (pink, with 0.3 added to make them comparable).

Figure 2 shows the outburst evolution from the *RXTE*/PCA X-ray data on a hardness-intensity diagram, where we plot the unabsorbed hardness ratios from 6–10 keV/3–6 keV, together with the unabsorbed 0.01–100 keV bolometric flux determined from the modelling. This reinforces the conclusions from the light curve and hardness ratios, that the source was in the very high state during T1–2 (red circle/orange square), then was in a bright soft state in T3 (green diamond), and a much dimmer soft state in T4 (blue triangle), while T5 (purple inverted triangle) was just before the transition back to the hard state.

3 SELECTION OF MULTI-WAVELENGTH SPECTRAL DATA

Our focus is to model the continuum emission over as broad a bandpass as possible. We extract the *HST* data from the Mikulski Archive for Space Telescopes (MAST) archive, removing any significant emission lines originating from the accretion disc (C IV (1550), He II (1640), He II (4686), H β ,

$H\alpha$ lines), as well as interstellar absorption lines (Si II, O I/Si II, C II, Ni III, Fe II, Fe II/Mn II, Mg II, Mg I lines), and the geocoronal Ly α line. We bin the remaining points to obtain better signal-to-noise. We then add 4% and 5% systematic errors to the MAMA data and the CCD data of *HST* spectra, respectively, considering the photometric accuracies.

We use the *RXTE* pipeline spectral products for the same dates corresponding to the *HST* data except for T5. As for T5, we instead use the nearest PCA data taken 5 days before the *HST* spectrum, considering the discussion in the preceding section. Also, we add 1% systematic errors to the spectral data between 3–25 keV. As for T4 and T5, we constrain the energy range to 3–15 keV.

We extend the wavelength coverage down to the IR regime by using simultaneous photometric points taken by the United Kingdom Infrared Telescope (UKIRT) 3.8-m telescope (Hynes et al. 2002). These are available for T1 (K band only), while T2 and T5 have *J*, *H*, and *K* bands.

4 MULTI-WAVELENGTH SPECTRAL MODEL: OPTXRPLIR

Fitting the optical/UV together with the X-ray spectral data from an accretion flow is not straightforward. There is an evolving series of broadband continuum SED models in the literature (Gierliński et al. 2009; Sutton et al. 2014; Shidatsu et al. 2016). We describe here the most recent version (the `optxrplir` model: Shidatsu et al. 2016) for completeness. Its relation to earlier models is discussed in Shidatsu et al. (2016).

The strength of irradiation of the outer parts of the accretion disc by the inner flow depends on the intrinsic illumination pattern of the X-ray source, the shape of the outer disc, and its albedo. The shape of the outer disc is itself dependent on the X-ray illumination, with Cunningham (1976) showing that this results in $H(R) \propto R^{9/7}$ so that $T_{\text{irr}}(R) \propto R^{-3/7}$, contrasting with the standard unilluminated disc where $H(R) \propto R^{9/8}$ and $T_{\text{visc}}(R) \propto R^{-3/4}$. Hynes et al. (2002) use these relations to make a simple irradiated disc model, where $T_{\text{eff}}^4(R) = T_{\text{visc}}^4(R) + T_{\text{irr}}^4(R)$. This is able to fit the optical/UV spectra, but does not match the simultaneous X-ray data (see Figure 5 of Hynes et al. 2002). There are several reasons for this, firstly the model only incorporates the disc emission, although black-hole binaries also show a power law which extends to significantly higher energies than expected for an optically thick disc. We assume that all the emission is powered by the standard Novikov-Thorne disc emissivity, and hence, the luminosity of the X-ray tail defines a radius, R_{pl} , below which the gravitational power released by accretion, must be dissipated in optically-thin material leading to Comptonisation, which is characterised by an electron temperature kT_{pl} and power-law spectral index Γ_{pl} , rather than making the highest temperature disc emission. The very high and intermediate states in black-hole binaries have additional lower temperature Comptonisation (e.g., Kubota & Done 2004), and hence, we similarly assume that this is powered by the luminosity released between R_{cor} and R_{pl} , which is characterised by an optical depth, τ and electron temperature kT_{warm} .

In addition, even where the high energy X-ray emis-

sion is low, containing less than 10% of the total emission, there is an offset in normalisation between the optical/UV emission from the outer disc and the X-ray emission from the inner disc (see e.g., the upper panel of Figure 5 in Hynes et al. 2002). This mismatch is due instead to the different temperature and density of the X-ray emitting inner disc compared to the optical emitting outer disc. The true absorption opacity can be much smaller than the electron scattering opacity, leading to a modified rather than true blackbody spectrum (Shakura & Sunyaev 1973; Czerny & Elvis 1987). This emission can be approximated as a colour temperature corrected blackbody, $B_{\nu}(f_{\text{col}}T_{\text{visc}})/f_{\text{col}}^4$, where f_{col} is a colour temperature correction factor which is ~ 1.6 – 2.6 at X-ray temperature but is ~ 1 at optical temperature (Shimura & Takahara 1995; Kubota et al. 2001; Davis & Hubeny 2006; Done et al. 2012; Shidatsu et al. 2016). We use the analytic approximation to $f_{\text{col}}(T_{\text{visc}})$ calculated in the Appendix of Davis & Hubeny (2006) as implemented in Done et al. (2012) for each annulus with $R > R_{\text{cor}}$. The lower line in the left panel of Figure 3 shows the resulting spectrum with only a fairly weak, hot corona ($R_{\text{cor}} = R_{\text{pl}} = 10R_{\text{g}}$) for $\log(L/L_{\text{Edd}}) = -1$. The hot Comptonisation region has $\Gamma_{\text{pl}} = 2.0$ and $kT_{\text{pl}} = 100$ keV, while the disc is assumed to extend to an outer radius $R_{\text{out}} = 10^5 R_{\text{g}}$. The break in shape of the disc emission between the optical and X-ray components is clearly evident.

We incorporate irradiation by assuming about the disc height that $H(R)/R = f_{\text{out}}(R/R_{\text{out}})^{2/7}$, where f_{out} sets the fraction of luminosity from the innermost radii which is intercepted by the outer disc. This is left as a free parameter rather than fixed to the self-consistent value in Cunningham (1976) to allow for additional effects such as scattering from a wind and/or limb darkening/brightening of the inner disc emission. The outer disc has some albedo a_{out} , so that only a fraction $(1 - a_{\text{out}})$ of the incident flux thermalises. We set $a_{\text{out}} = 0.9$ on the assumption that the skin of the outer disc is highly ionised by the X-ray illumination (van Paradijs & McClintock 1994; Jimenez-Garate et al. 2002). The left panel in Figure 3 shows the change in optical/UV emission in increasing f_{out} from zero (the intrinsic emission from the accretion flow) to 4×10^{-2} , where irradiation is important. The middle panel in Figure 3 shows the expected change as a function of increasing L/L_{Edd} , showing how the level of the IR/optical emission on the Rayleigh-Jeans tail has only a small dependence on the total luminosity ($\propto L^{1/4}$). The right panel of Figure 3 shows that this lowest energy emission is much more sensitive to the size scale of the outer disc.

5 CONSTRAINING PARAMETERS IN BROADBAND FITTING WITH OPTXRPLIR

The model `optxrplir` contains the black-hole mass and the distance to the object as free parameters. We constrain the range of the black-hole mass to 6.16 – $15.5 M_{\odot}$ (Corral-Santana et al. 2011) and fix the distance of 8 kpc (Hynes 2005; Tetarenko et al. 2016). The black-hole spin parameter a_* is fixed to 0. This model assumes a 60-degree inclination in computing the disc spectrum. We fix the normalisation to 1, since the inclination of this object is suggested to be close to 60 deg (Corral-Santana et al. 2011).

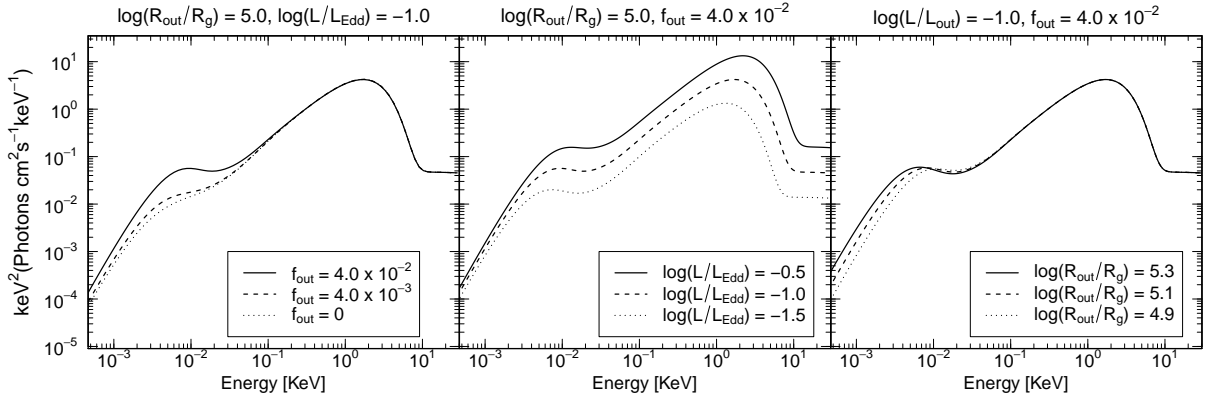


Figure 3. Model emission of the irradiated disc in the `optxrlir` model as a function of disc height (left panel), or luminosity (middle panel), or outer disc radius (right panel). Here, $r_{\text{cor}} = r_{\text{pl}}$, and the parameters r_{pl} and Γ are fixed to 8 and 2.0, respectively. The other fixed parameters are the same as those described in Sec. 4.1.

At this inclination and spin, the Doppler boosting of the inner disc emission is almost completely offset by gravitational redshift, and hence, we do not impose any relativistic corrections. We also fix the temperature of the hot corona at 100 keV, which is much higher than the energy range of *RXTE*/PCA data.

There can also be reflection of the Comptonisation components from the inner disc. We model this in an approximate way using `smedge`, with the cross-section index fixed at -2.67 . We also include a constant component from the companion star as a blackbody (`bbodyrad`). The companion star in this object is a K late-type star according to Corral-Santana et al. (2011), and has temperature in the range of $3.2\text{--}3.6 \times 10^4$ keV and radius of $4.5\text{--}6.2 \times 10^5$ km (Allen 1973).

To fit the raw data requires that we include reddening and absorption from dust and gas in the interstellar medium (ISM). We use the `phabs` model for the gas phase as it does not include the neutral edges below 13.6 eV (e.g., from Fe I). These are not present in our data at the expected level from neutral material due to the multiphase nature of the ISM, where most Fe is ionised to Fe II. We constrain N_{H} in the gas phase to the range $1.0\text{--}3.0 \times 10^{21}$ cm^{-2} by using *ASCA*/GIS data on MJD 51474. This extends down below 1 keV and is more sensitive to absorption than the *RXTE*/PCA.

There is a range of UV reddening curves, all of which are subtly different especially around the 2200Å feature (Fitzpatrick 1999; Cardelli et al. 1989; Seaton 1979). Hynes (2005) used the reddening curve of Fitzpatrick (1999), and showed that the optical/UV data are significantly curved, but we use that of Seaton (1979) as this is readily available in XSPEC. This only extends down to 3700Å (3.4 eV), and hence, we only include the shorter wavelength *HST* data. The data above 3500Å, we apply the averaged curve of Cardelli et al. (1989), after checking that the two extinction laws give the same reddening within a few percent above 3500Å (Fitzpatrick & Massa 2007).

We fit all 5 spectra simultaneously from 0.0034–25 keV, with the model `uvred*phabs*smedge*(bbodyrad+optxrlir)`, before fitting individually. The black hole mass, the companion star parameters, the N_{H} and $E(B - V)$ are tied across all the

datasets. The best-fit values are $6.9 M_{\odot}$ for the black-hole mass, 3.6×10^{-4} keV, and 6.2×10^5 km for the temperature and radius of the companion star, 3.0×10^{21} cm^{-2} for the interstellar Hydrogen column density and 0.527 for $E(B - V)$. The different value of $E(B - V)$ between Hynes et al. (2002) and our paper is attributed to the difference in the reddening curve described in the preceding paragraph. We note that this black hole mass, as well as being consistent with previous determinations, gives the luminosity just before the soft-to-hard transition of around 2% of the Eddington luminosity, as expected from the advection-dominated accretion flow models of the low/hard state (ADAF; Narayan & Yi 1995), and in line with what is generally observed (Maccarone 2003).

6 EVOLUTION OF THE ACCRETION FLOW

In this section, we fit the spectra at each epoch (T1–5) individually, using the model `phabs*smedge*(bbodyrad+optxrlir)`. Then we fix all the system parameters at these best fit values in the preceding section in order to better constrain the remaining parameters of the accretion flow. We also de-redden the IR/optical/UV data with the estimated $E(B - V)$ value described in the previous section. The `phabs` absorption applies only to the X-ray data to correct for this X-ray absorption. We give the de-convolved, de-absorbed SED in the top window in Figure 4, and show residuals to the best fit model in the small window below each spectrum.

6.1 Modelling of the Very High State at the Early Stage

The hardness-intensity diagram (see Figure 2) clearly shows that the X-ray spectra in T1 and T2 are in the very high state. This state can show strong low-temperature and optically-thick thermal Comptonisation as well as a power law tail to higher energies indicating a hotter, optically-thin component (e.g., Życki et al. 2001; Kubota et al. 2001; Kubota & Done 2004). We deal with this component by al-

lowing R_{cor} to be a separate free parameter, along with the electron temperature and optical depth of this component.

The initial fit of this baseline model to T1 and T2 shows an excellent match to the optical/X-ray spectra in the upper two panels of Figure 4, but with a strong IR excess. This is most clearly seen in T2 where there are IR data across J , H and K bands. This could indicate a contribution from the radio jet. This is known to closely follow the hard X-ray Comptonised flux, even into the soft states (Zdziarski et al. 2011). The very high and intermediate states are often the ones with the strongest jet emission (Fender et al. 2004), and radio monitoring of XTE J1859+226 during this outburst showed that the radio luminosity was largest in these initial stages of the outburst (Brocksopp et al. 2002). We thus add a power law to approximately model the synchrotron jet emission. This gives a much better fit to the IR region, without changing the fit at higher energies (see the lower windows of the upper two panels in Figure 4). The jet makes a 20–30% contribution to the IR flux, with a rather steep synchrotron emission index of ~ 2.5 , which is consistent with the IR jet emission seen in GX 339–4, another black-hole LMXB (Gandhi et al. 2011). The best-fit parameters and their errors are given in Table 1.

6.2 Modelling of the High/Soft States

The X-ray spectra in T3 and T4 are clearly in the high/soft state according to the hardness-intensity diagram (see Figure 2). Hence we do not include the low-temperature Comptonization component that is considered in modelling of SEDs in the very high state in the previous subsection, i.e., we set $R_{\text{pl}} = R_{\text{cor}}$. We also now include a gaussian line with upper limit on the width of 0.5 keV as there are small but significant residuals in the 6–7 keV bandpass which indicate that the phenomenological `smedge` model is not sufficient to describe the reflection spectrum from the inner disc in these data.

The best-fit SEDs for T3 and T4 are shown in the middle panels in Figure 4, and the best-fit parameters are given in Table 1. The X-ray spectra are well reproduced by dominant disc emission, with a weak power-law Comptonised tail, and a small contribution from the iron line for both high/soft state SEDs.

The UV and optical spectra for T3, taken only 10 days after the very high state and at similar luminosity, are well fit by the expected irradiated disc emission. However, the optical/UV spectra of T4, taken about three months after T3 with order of magnitude lower luminosity, shows small but significant deviations away from the irradiated disc model, despite both the outer disc radius and height being free to vary. The best-fit values of both these parameters are different from those of T1–3, with the disc outer radius being significantly smaller and the disc height being significantly larger. The fit is, however, quite poor, with χ^2/dof larger than 2, and thus, the error ranges on the parameters may not be reliable.

6.3 Modelling near the Transition to the Low/Hard State

The spectrum T5 is the lowest luminosity spectrum, taken just before the transition back to the low/hard state (Figure

2). This is adequately fitted using only the `smedge` to model the reflection features, and does not require the separate Fe line emission. The resulting SED is represented in the bottom panel of Figure 4, and we can see the multi-wavelength fit is very poor.

Given that the X-rays are not strictly simultaneous in these data, and that the source was clearly in the low/hard state 4 days later, it is possible that the source was already in the low/hard state during the time of the T5 spectra. Thus there could be a potential component from the jet as well as from an irradiated disc. However, the jet should contribute more in the IR emission, similar to T1–2, whereas the IR flux level is clearly fairly well matched by the data.

Again, the best fit values of disc outer radius and height are different from those of T1–3, with the disc outer radius being significantly smaller, similar to T4. However, as shown by the residuals, the fit is now extremely poor, with $\chi^2/\text{dof} \sim 10$. Some of this may be due to intrinsic variability giving a different normalisation between the four *HST* wavelength ranges, but plainly the main issue is the lack of spectral curvature in the optical/UV regime compared to that predicted for an irradiated disc. This change in curvature in the optical/UV spectra for T1–3 compared to T5 is irrespective of the X-ray data, e.g., see the de-reddened *HST* spectra of Figure 4 in Hynes et al. (2002).

6.4 Changing Optical/UV Spectral Shape

We focus on the changing optical/UV spectral shape between the classic irradiated disc shape in T1–3 (described as UV soft spectra in Hynes et al. 2002) to the less curved shape of T4 and especially T5 (UV hard, Hynes et al. 2002). We look at this in a model independent way by computing the ratio of optical/UV data from the accretion flow in each epoch. We subtract the contribution of the companion star from each spectrum, and then estimate the ratios between the resultant fluxes. The ratio of T2/T1 is R12, the ratio of T3/T2 is R23 etc. These flux ratios are shown as a function of energy in Figure 5. These show that R12 and R23 are slightly decreasing with increasing energy across the optical/UV band as expected for constant outer disc radius with slightly decreasing illuminating flux and bolometric luminosity (see also the left and middle panels of Figure 3).

The large drop in flux between T3 and T4 is evident in the much lower normalisation of R34, but the flux ratio between these two widely separated epochs is unexpectedly fairly constant with energy. The model spectra shown in the middle panel of Figure 3 shows how the irradiated disc spectrum in the `optxrplir` model changes with changing only $\log(L/L_{\text{Edd}})$, and this clearly makes much more impact on the UV flux than on the optical flux; however, the R34 ratio is mostly flat across this entire range. Instead, in the context of the irradiated disc models, to decrease the optical flux requires a smaller R_{out} (see also the right panel of Figure 3).

We explore whether a decrease in $\log(L/L_{\text{Edd}})$ and R_{out} can explain most of the observed change in optical/UV emission in T4. We fit the SED in T4 with f_{out} fixed to 4.0×10^{-2} similar to T1–3. While the resulting fit, shown in the left panel of Figure 6, has the same drop in $\log(L/L_{\text{Edd}})$ and $\log(R_{\text{out}})$ as in the fit with a free f_{out} , this gives a better match to the optical data than the fit allowing f_{out} to be

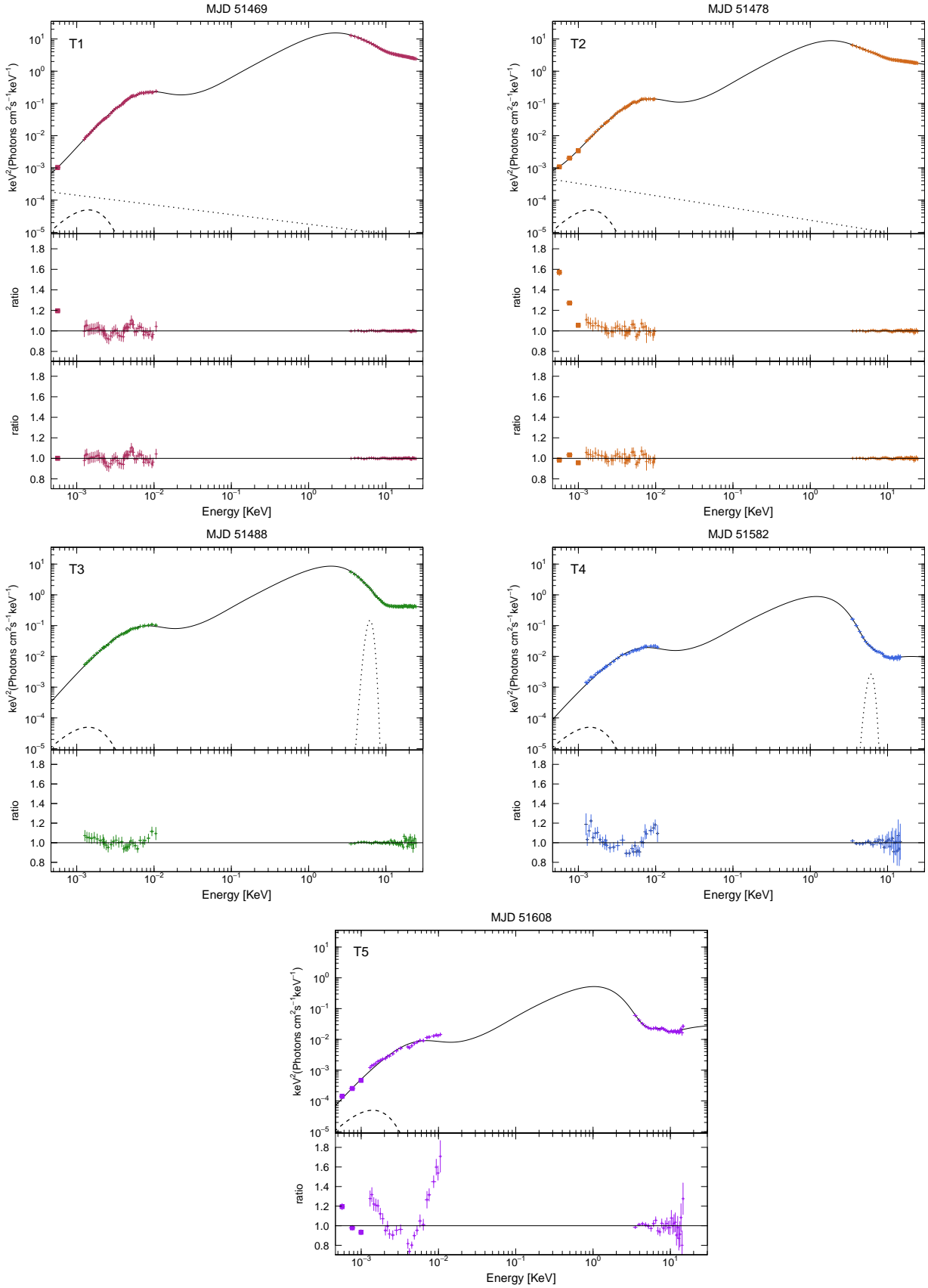


Figure 4. Multi-wavelength SEDs and their ratios on T1–T5. On T1 and T2, we prepare the ratio without a power-law model for comparison in the middle windows. The crosses and solid line represent the observed SED and the emission reproduced by our model, respectively. The rectangles are the IR data. The dashed line represents the emission from the companion star. The dot line in the upper panels represents the model emission from synchrotron jet ejection, and that in the middle panels represents the model emission from

Table 1. Best-fit parameters of our modelling in the 5 sets of broad-band spectra.

| Model | Parameter | T1 | T2 | T3 | T4 | T5 |
|---------------------|---|----------------------------|----------------------------|----------------------------|----------------------------|----------------------------|
| smedge | E_c^* | 7.6±1.1 | 7.4±1.0 | 8.4±0.3 | 8.3±1.7 | 8.1±0.6 |
| | f^\dagger | 0.29±0.71 | 0.5±0.5 | 1.0±0.3 | 1.0±0.7 | 1.0±0.6 |
| | W^\ddagger | 4.7±34 | 5.6±11.3 | 4.5±1.4 | 2.3±1.2 | 2.7±2.2 |
| gaussian | E_1^\S | – | – | 6.1±0.3 | 6.0±0.4 | – |
| | σ^\P | – | – | 0.50±0.06 | 0.5±0.5 | – |
| | N_1^\l | – | – | (4.9±1.5)×10 ⁻³ | (0.9±6.0)×10 ⁻⁵ | – |
| pegpwlw | α^{**} | 2.3±2.8 | 2.4±0.6 | – | – | – |
| | $N_2^{\dagger\dagger}$ | 0.65±0.53 | 1.4±0.7 | – | – | – |
| optxrplir | $\log(L/L_{\text{Edd}})^{\ddagger\ddagger}$ | -0.38±0.09 | -0.59±0.02 | -0.68±0.01 | -1.67±0.01 | -1.88±0.02 |
| | $R_{\text{cor}}^{\S\S}$ | 32±50 | 22±300 | – | – | – |
| | $\log(R_{\text{out}}/R_g)^{\P\P}$ | 5.26±0.01 | 5.23±0.02 | 5.20±0.01 | 4.92±0.02 | 4.91±0.01 |
| | $kT_{\text{es}}^{\l\l}$ | 1.06±0.16 | 1.1±0.4 | – | – | – |
| | τ^{***} | $\gtrsim 7.3$ | $\gtrsim 4.7$ | – | – | – |
| | $R_{\text{pl}}^{\dagger\dagger\dagger}$ | 19±9 | 19±1 | 10.30±0.06 | 8.22±0.25 | 10.81±0.57 |
| | $\Gamma^{\ddagger\ddagger\ddagger}$ | 2.42±0.07 | 2.30±0.06 | 2.17±0.04 | 2.16±0.24 | 1.83±0.13 |
| | $f_{\text{out}}^{\S\S\S}$ | (4.4±0.8)×10 ⁻² | (4.0±0.3)×10 ⁻² | (3.2±0.1)×10 ⁻² | (6.2±0.3)×10 ⁻² | (4.0±0.4)×10 ⁻² |
| χ^2/dof | 0.47 | 0.63 | 0.99 | 2.26 | 10.47 | |

*Threshold energy of reflection in units of keV.

†Maximum absorption factor at the threshold energy.

‡Smearing width in units of keV.

§Line energy in unit of keV.

¶Line width in unit of keV.

⌌Total photons/cm⁻²/s in the line of sight.

**Photon index of power law α .

††Flux in units of 10⁻¹² ergs/cm²/s over the energy range (0.0005–0.02 keV).

‡‡Luminosity divided by the Eddington luminosity in logarithmic scales.

§§Radius of the low-temperature Comptonization component in units of R_g .

¶¶Disc radius in units of R_g in logarithmic scales.

⌌⌌Temperature of the low-temperature Comptonization component in units of keV.

***Optical depth in the low-temperature Comptonization component.

†††Radius of the central hot corona in units of R_g .

‡‡‡Photon index of the central hot corona.

§§§Geometry-dependent factor of the thermalized fraction at the illuminated outer disc.

free (the right middle panel of Figure 4), but a dramatically worse fit to the UV spectra (see the left panel of Figure 6). The dashed-dotted line shows keeping $\log(R_{\text{out}})$ fixed at 5.2 as in T3, showing how the optical data strongly require a decrease in R_{out} to compensate for the change in $\log(L/L_{\text{Edd}})$, but that this alone does not have the correct shape. The *HST* data in T4 can instead be fitted by ignoring the simultaneous X-ray data, i.e., by assuming that the disc is not in steady state. The right panel of Figure 6 shows how the curvature across the entire optical/UV bandpass can be fitted by assuming almost very weak illumination of a disc with a higher mass accretion rate than that consistent with the X-ray emission. The curvature in the UV region is then almost entirely from the increasing colour temperature correction rather than from irradiation. The disc outer radius is again significantly smaller than in T1–3. The estimated parameters in these additional two SED fittings are given in Table 2. Thus there is a potential solution to explain the shape of the *HST* spectrum in T4 if the outer disc is intrinsically hotter than that expected from the mass accretion rate as measured from the inner disc.

The break in behaviour from T1–3 is even more marked in T5. The ratio R45 clearly has a strong energy dependence,

with the UV flux changing by more than the optical flux (see the bottom panel of Figure 5). We try two additional modellings on T5 as well as them on T4 in the preceding paragraph, and fail to fit the excess properly in fitting the broadband data simultaneously. When we fix $\log(R_{\text{out}}/R_g)$ to 5.0 and f_{out} to 4.0×10^{-2} , the excess at the optical and IR flux becomes within ~20%; however, it does not completely disappear and the excess at the UV flux becomes larger than the modelling shown in the bottom panel of Figure 4 (see the left panel of Figure 7). The right panel of Figure 7 shows the result of fitting to the UV/optical/IR data without including the X-ray emission, i.e., allowing the disc to be non-steady state. We get a much better fit to the curvature in the optical/UV spectra by an unirradiated, but hotter intrinsic outer disc, with $\log(R_{\text{out}}/R_g) \sim 5.0$ as well as T4. Then, the best-fit values of $\log(L/L_{\text{Edd}})$ and f_{out} are -1.09 and 1.1×10^{-8} , respectively. However, the fit here is never statistically acceptable unlike that in T4. The χ^2/dof is equal to 6.9, though the residuals are less than ~20%, and could be potentially produced by variability between different wavelength *HST* ranges. X-ray spectral changes are most rapid around the transition (see e.g., Dunn et al. 2010), which would mean that the reprocessed flux could

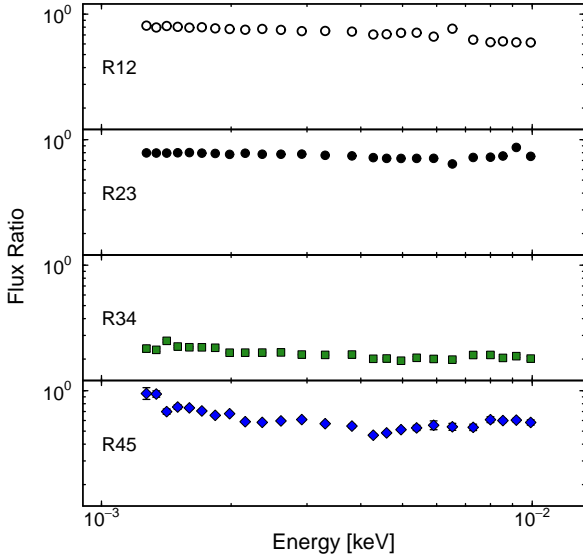


Figure 5. Flux ratio of the UV and optical spectra taken by *HST* between two adjacent time zones.

also change rapidly. Nonetheless, the optical/UV spectra are better matched by the intrinsic disc emission than by reprocessed flux, but if this is intrinsic flux then the level implies a mass accretion rate through the outer disc is ~ 5 times larger than that in the inner disc.

Table 2. Best-fit parameters of our additional SED modellings on T4. See the notations in Table 1 for the notation of each parameter.

| Model | Parameter | T4 (f_{out} fix) | T4 (only <i>HST</i> spectra) |
|----------|-------------------------------------|----------------------------|--------------------------------|
| optxplir | $\log(L/L_{\text{Edd}})$ | -1.67 | -0.80 ± 0.08 |
| | $\log(R_{\text{out}}/R_{\text{g}})$ | 5.01 ± 0.01 | 5.00 ± 0.03 |
| | f_{out} | 4.0×10^{-2} (fix) | $(1.8 \pm 1.4) \times 10^{-3}$ |

7 DISCUSSION

7.1 Time Evolution of Irradiation Effect

The UV/optical/IR spectra on T1–3 are mainly explained by the canonical irradiation in our model (see also Sec. 6.1–6.2), although the IR emission requires an additional component, probably from the jet, in T1 and T2. The amount of irradiation drops by 25% as the source luminosity declines by a factor of 2 from T1 to T3. By contrast, our irradiation model fails to match the shape of the UV/optical spectra together with the X-ray spectra in the late stage of the outburst (T4–5, see also Sec. 6.2–6.4). We firstly investigate theoretical ideas of how the irradiation should change, and then apply them to our data.

7.1.1 Theoretical Models of Irradiation

Here, we consider the structure of the irradiated disc to see if the observed f_{out} values can be matched by theoretical predictions. At first, we consider the irradiated disc model of Cunningham (1976). This has a prediction for the scale height of the outer disc when irradiation dominates. Recasting their equation (27c) into the units used here, gives

$$\begin{aligned} H/R &= 1.5 \times 10^{-3} (L/L_{\text{Edd}})^{1/7} (M_{\text{BH}}/M_{\odot})^{-1/7} (R_{\text{out}}/R_{\text{g}})^{2/7} (R/R_{\text{out}})^{2/7} \\ &= f_{\text{d,out}} (R/R_{\text{out}})^{2/7}. \end{aligned}$$

Since this was derived by assuming 1/3 of the flux thermalises in the disc, which is slightly larger than the $(1-a) = 0.1$ assumed here, this will slightly overestimate f_{out} . This predicts a rather small change of around 10% in f_{out} as the source flux drops by a factor 2 from T1–3, as observed, but the calculated values underestimate f_{out} by around a factor 2, suggesting that there is an additional source of irradiation of the outer disc as well as direct illumination.

Begelman et al. (1983) show that irradiation also forms a static coronal atmosphere over the inner disc, which can escape as a thermal wind at large radii. The static coronal material is heated to the inverse Compton temperature, $kT_{\text{IC}} = \frac{1}{4} \int EL(E)dE / \int L(E)dE$, which depends only on the shape of the radiation field and not on its luminosity. We take 100 keV as the upper limit of the integrals to account for the Klein-Nisina rollover in electron scattering cross-section. When the sound speed of the Compton heated material, c_{IC} , exceeds the escape velocity at $R_{\text{IC}} = GM/c_{\text{IC}}^2$, a wind can be launched. However, the wind is outflowing, and hence, there is finite time for heating. The wind will not fully reach T_{IC} at R_{IC} if the luminosity is below the critical luminosity $L_{\text{crit}} \approx 0.03 T_{\text{IC},8}^{-1/2} L_{\text{Edd}}$ (Done et al. 2018; Begelman et al. 1983, where $T_{\text{IC},8} = T_{\text{IC}}/10^8$ K). Instead, it is only heated to a characteristic temperature $T_{\text{ch}} < T_{\text{IC}}$, and hence, the transition between the wind and atmosphere takes place at $R \sim (L/L_{\text{crit}})^{-1} R_{\text{IC}}$ (with some dependence on Compton temperature, Woods et al. 1996; Higginbottom & Proga 2015; Done et al. 2018). A more careful treatment shows that the material escapes as a wind when $R_{\text{in}} > 0.2 R_{\text{IC}}$ for $L > L_{\text{crit}}$, and when $R_{\text{in}} > 0.2 (L/L_{\text{crit}})^{-1} R_{\text{IC}}$ for $L < L_{\text{crit}}$.

The corona and wind form two separate scattering regions. Begelman & McKee (1983) determine the scattered luminosity from the coronal region (their equation (3.15)) as

$$\frac{L_{\text{sc}}}{L} \approx 0.19 \left(\frac{T_{\text{IC},8} (L/L_{\text{Edd}})}{\Xi_{\text{h,min}} \epsilon_{-1}} \right)^{1/4},$$

where ϵ_{-1} is the efficiency scaled to 0.1, so that $L = (0.1 \epsilon_{-1}) M c^2$, and $\Xi_{\text{h,min}} \sim 40$ is the minimum ionisation parameter for the hot phase of the thermal instability curve (Begelman et al. 1983). This is insensitive to the source parameters such as disc size as it occurs primarily at small radii where the density in the corona is highest. Since we assume $\epsilon_{-1} = 0.57$ (zero spin black hole), $L_{\text{sc}}/L = 0.08 [T_{\text{IC},8} (L/L_{\text{Edd}})]^{1/4}$. The coronal scattering is maximised at the radius of the inner attenuation zone, R_{ia} , it has typical height $H_{\text{c}}(R_{\text{ia}}) = [2(R_{\text{ia}}/R_{\text{IC}})^3]^{1/2} R_{\text{IC}} \sim 0.7 (L_{\text{sc}}/L)^3 R_{\text{IC}}$ (Begelman & McKee 1983, their equations (2.6) and (2.23)). This is always fairly small, of order a few tens of R_{g} for T1–3 and even smaller for T4–5, so this coronal scattering region is not a major source of illumination for the outer disc.

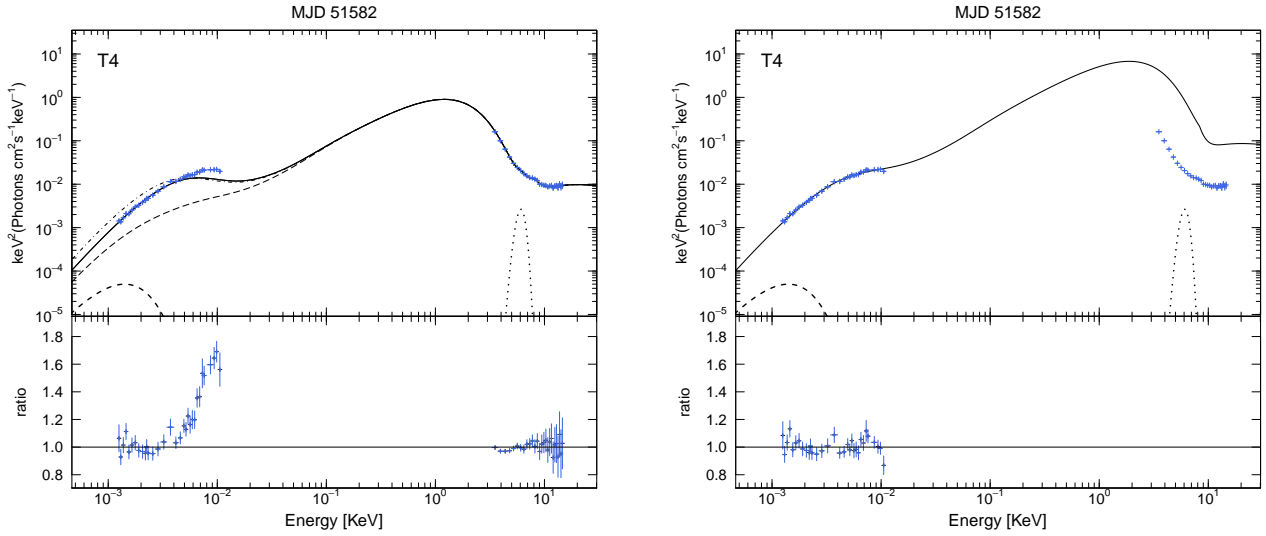


Figure 6. Multi-wavelength SED modeling and the ratio of SED on T4 with f_{out} fixed to 4.0×10^{-2} (left panel), and those without the X-ray spectra (right panel). The crosses and solid line represent the observed SED and the emission reproduced by our model, respectively. The dashed and dot lines represent the emission from the companion star and that from iron line, respectively. The dash-dotted line in the left panel is the model with $\log(R_{\text{out}}/R_{\text{g}}) = 5.2$. The long-dashed line in the left panel represents an unirradiated disc.

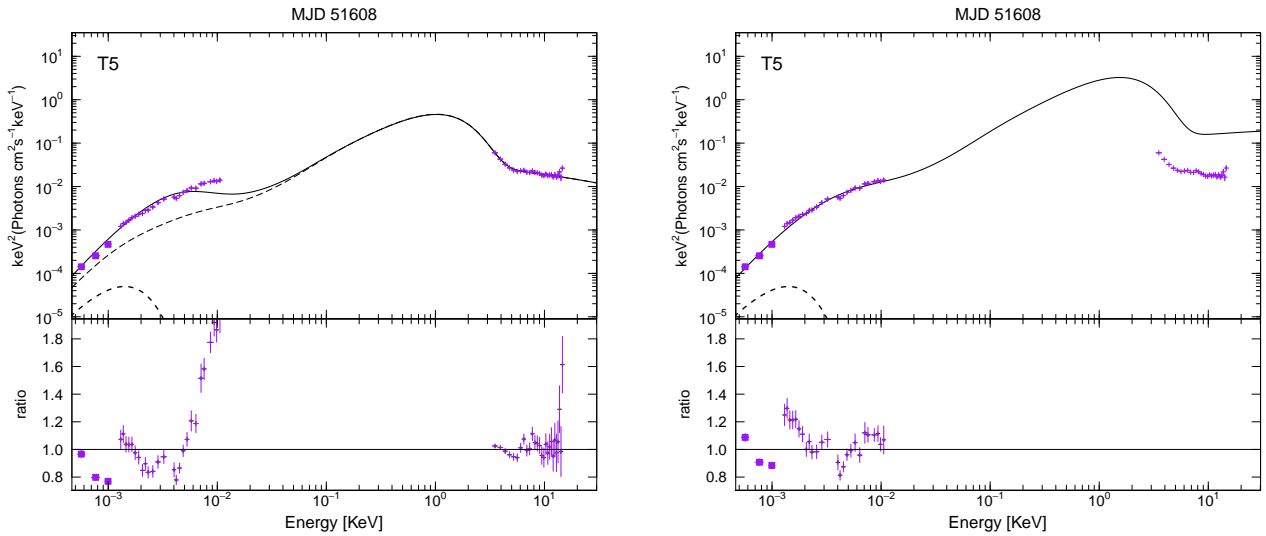


Figure 7. Multi-wavelength SED modeling and the ratio of SED on T5 with fixed f_{out} and $\log(R_{\text{out}}/R_{\text{g}})$ (left panel) and those without the X-ray data (right panel). The crosses and solid line represent the observed SED and the emission reproduced by our model, respectively. The rectangles are the IR data. The dashed line represents the emission from the companion star. The long-dashed line in the left panel represents an unirradiated disc.

However, there is also scattering from the wind, which is maximised at the launch radius R_{in} , with typical height $H_{\text{w}}(R_{\text{in}}) \approx R_{\text{in}}$, which forms an additional component which is much more efficient at illuminating the outer disc. This gives a scattered luminosity

$$\frac{L_{\text{sc}}(\text{wind})}{L} = \frac{L}{L_{\text{Edd}} \Xi_{\text{c,max}}} \begin{cases} 0.5 & \text{(A)} \\ \left(\frac{L_{\text{crit}}}{L}\right)^{2/3} [11 - 7(R_{\text{out}}/R_{\text{IC}})] & \text{(B)} \\ 9[1 + \ln(R_{\text{out}}/R_{\text{IC}})] & \text{(C)} \end{cases}$$

for wind regions A, B and C, respectively (Begelman & McKee 1983, their equation (3.9)), where

$\Xi_{\text{c,max}} \approx 10$ is the maximum ionisation parameter on the cold branch. We note that this approximation is not piecewise continuous, nor does it not take into account the increase in the wind mass loss expected as the source approaches L_{Edd} due to the significant radiation pressure.

Thus there are potentially three components to the flux seen by the outer disc. One of them is direct illumination from the central source, which depends on the flaring of the disc and is $\propto H_{\text{d}}/R$, and the others are from scattering in the corona $\propto L_{\text{sc}}(\text{corona})(H_{\text{c}}/R)$ (generally negligible), and from scattering in the wind $\propto L_{\text{sc}}(\text{wind})(H_{\text{w}}/R)$. Thus the total flux

seen by the outer disc can be approximated by an effective $f_{\text{out}} \approx f_{\text{d,out}} + L_{\text{sc}}(\text{wind})/L$.

7.1.2 Application to XTE J1859+226

We evaluate T_{IC} from the spectral shape for T1–5, and use this to derive L_{crit} and R_{IC} for all of our datasets. We tabulate the predicted thermal corona/wind parameters in Table 3. There is a marked drop in T_{IC} linked to an increase in L_{crit} and R_{IC} as the source softens from the very high state at T1–2 to the bright high/soft state T3, but all these bright spectra (T1–3) have $L > L_{\text{crit}}$, and hence have a wind region which starts at $R_{\text{in}} = 0.2R_{\text{IC}}$. Also, the wind region is A, since $R_{\text{iso}} > R_{\text{out}} > R_{\text{IC}}$ at the outer disc radius.¹ The ignition radius of the wind is just within the outer region of the disc in these data, but the expected mass loss rate is fairly low as the outer disc radius is fairly small. The coronal scattering is negligible, since R_{ia} and $H_{\text{c}}(R_{\text{ia}})$ are quite small. The values for f_{out} from theoretical models of scale height of the irradiated outer disc and scattering from the wind are remarkably close to those observed in T1–3, though the albedo of the wind may be slightly higher than our assumed value of 0.9, and though the scale height of the outer disc is overestimated (see the discussion in Sec. 7.1.1). Importantly, the models predict similar decrease in f_{out} as seen in the data as the source flux and $T_{\text{ic},8}$ drop from T1 to T3.

Conversely, T4 has a much lower luminosity. It is still disc dominated, but T_{IC} is low because the disc is cooler, and $R_{\text{in}} > R_{\text{out}}$ because of $L < L_{\text{crit}}$. Thus there should be no wind region, only a static corona heated to T_{IC} . Also, T5 is similarly low luminosity, though the X-ray tail is somewhat stronger (though quite poorly constrained), giving T_{IC} which is comparable to T3. However, the lower luminosity again means that $L < L_{\text{crit}}$ and $R_{\text{in}} > R_{\text{out}}$. The coronal scattering is negligible as well as in T1–3. Scale height of the irradiated outer disc should give a much smaller f_{out} in these spectra than in T1–3, yet instead the data require a much larger f_{out} in order to (poorly) fit the observational UV flux under the assumption of steady state in fitting broadband data simultaneously (see also Sec. 6.3 and 6.4). This could instead indicate that there is an additional component in the optical/UV spectrum. However, T4 is still clearly in the disc dominated high/soft state, and hence, a jet component is not likely, and indeed the IR points in T5 do not indicate any such emission. Instead, T4 and T5 have differently shaped UV spectra (hard rather than soft, see also Hynes et al. 2002) which are better fitted by a rather different disc model, where the intrinsic heating of the outer disc is larger than in the inner regions.

7.1.3 Application to a Canonical Outburst

We calculate the evolution of the irradiation controlled shape of the disc for a canonical outburst in Figure 8. We assume the same parameterisation as in Done et al. (2018), where the hard state, low luminosity spectra ($L \leq 0.02L_{\text{Edd}}$) are assumed to have $T_{\text{ic},8} = 0.88 - 0.46 \times \log_{10}[L/0.002L_{\text{Edd}}]$, while the soft, higher luminosity spectra are assumed to

¹ Here, R_{iso} is defined as $R_{\text{IC}}(L/L_{\text{crit}})$ by equation (2.15) in Begelman et al. (1983).

Table 3. Thermal corona/wind parameters in T1–5. We use the luminosity and R_{out} summarised in Table 1 in these calculations.

| Parameters | T1 | T2 | T3 | T4 | T5 |
|--|-------------------|-------------------|-------------------|---------|---------|
| T_{IC}^* | 1.44 | 1.65 | 0.85 | 0.38 | 0.80 |
| $R_{\text{in}}/R_{\text{g}}^\dagger$ | 8.0×10^4 | 7.0×10^4 | 1.3×10^5 | no wind | no wind |
| $L_{\text{est}}/L_{\text{crit}}^\ddagger$ | 5.7 | 3.7 | 2.2 | 0.15 | 0.13 |
| $\dot{M}_{\text{wind}}/\dot{M}_{\text{acc}}^\S$ | 0.29 | 0.31 | 0.09 | – | – |
| $f_{\text{d,out}}^\parallel$ | 0.032 | 0.029 | 0.028 | 0.017 | 0.016 |
| R_{ia}^\lrcorner | 445 | 326 | 410 | 196 | 106 |
| $H_{\text{c}}(R_{\text{ia}})^{**}$ | 21 | 14 | 15 | 3.2 | 1.9 |
| $L_{\text{sc,wind}}/L_{\text{est}}^{\dagger\dagger}$ | 0.021 | 0.013 | 0.010 | – | – |
| $f_{\text{out}}^{\ddagger\dagger}$ | 0.053 | 0.050 | 0.041 | 0.017 | 0.016 |

*Inverse-Compton temperature estimated from the spectral shape. In units of keV.

[†]Innermost radius where the wind is efficient.

[‡]Ratio of the estimated luminosity against the critical luminosity, with which the wind can be triggered.

[§]Ratio of the wind accretion against the whole accretion rate.

[∥]Scale height of an outer disc defined by equation (27c) in Cunningham (1976).

[⌞]Radius of an inner attenuation zone derived from equation (2.23) in Begelman & McKee (1983).

^{**}Typical height of an inner attenuation zone derived from equation (2.6) and R_{ia} in Begelman & McKee (1983).

^{††}Scattered luminosity from a wind according to equation (3.9) in Begelman & McKee (1983).

^{‡‡}Predicted total f_{out} estimated by $f_{\text{d,out}} + L_{\text{sc,wind}}/L_{\text{est}}$.

be disc dominated with $T_{\text{ic},8} = 0.036[L/0.02L_{\text{Edd}}]^{1/4}$, respectively, for a fixed $R_{\text{out}} = 10^{6.3}R_{\text{g}}$. There is a very small but systematic increase in $f_{\text{d,out}}$ with L/L_{Edd} (panel b), while the wind scattered fraction (panel d) is clearly affected by the analytic approximations used, but is of the same order as $f_{\text{d,out}}$, so that the total f_{out} should be a slowly increasing function of L/L_{Edd} . This gives a way to quantify the effect of X-ray illumination in the disc instability model, removing a major uncertainty in current calculations (Tetarenko et al. 2018).

7.2 Time Evolution of Outer Disc Radius

Another key difference between T1–3 and T4–5 is that the disc outer radius has clearly decreased (see also Hynes et al. 2002). Some disc shrinkage is expected in the standard irradiated disc instability model (Dubus et al. 2001), but not as much as the factor 2 seen in these data. However, we can understand the degree of shrinkage by considering that disc extended much larger at the initial stage of the outburst than expected by the thermal instability. The thermal-tidal instability in low mass ratio objects makes it possible (Ichikawa et al. 1993).

XTE J1859+226 has an extremely small mass ratio, $q = M_2/M_{\text{BH}} \sim 0.09$, and its orbital period is 6.6 hours (Corral-Santana et al. 2011). In this system, the disc radius will definitely exceed the 3:1 resonance radius, $\sim 0.47a^2$ by thermal-tidal instability. This instability was originally proposed in SU UMa-type dwarf novae which typically have $q \lesssim 0.25$ and orbital periods of a few hours, and the similarities between SU UMa-type objects and some of

² Here, a is the binary separation.

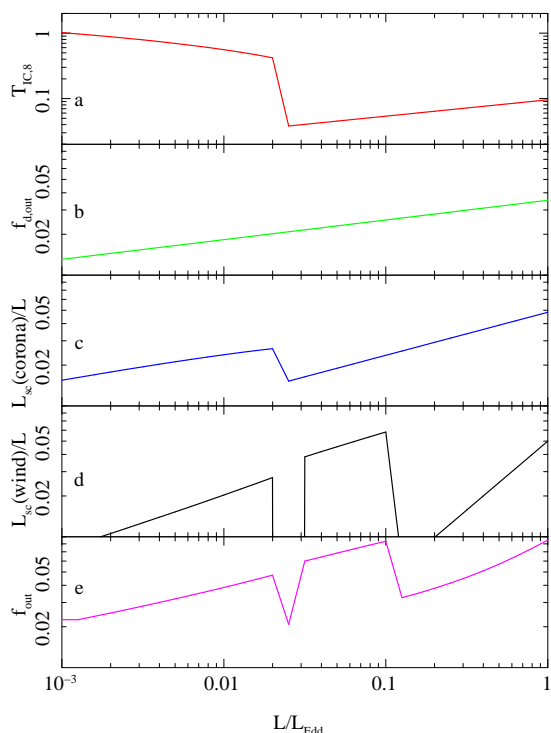


Figure 8. a) The dependence of the inverse Compton temperature with luminosity for a canonical outburst which switches from power law dominated to disc dominated at $0.02L_{\text{Edd}}$. b) This predicts the solid angle of the disc assuming direct irradiation, c) the scattered fraction from the static corona and d) the scattered fraction from the wind. The wind approximation is clearly not piecewise continuous. e) The total irradiation of the outer disc. This is the combination of direct illumination and scattering in the wind as the corona radius and scale height are too small to have a large effect on the outer disc.

LMXBs have been pointed out (e.g., [Kato et al. 1995](#)). The 3:1 resonance begins growing at the onset of the outburst ([Osaki 1989](#)), and slowly results in the outer disc becoming elliptical, producing superhumps with a period which is slightly longer than the orbital period. XTE J1859+226 also showed superhump candidates during the 1999–2000 outburst ([Uemura et al. 2004](#)). In WZ Sge-type dwarf novae, an extreme subclass of SU UMa-type dwarf novae, with $q \lesssim 0.08$, the 2:1 resonance can work in the initial stage of outbursts, and it has a shorter growth time than the 3:1 resonance ([Osaki & Meyer 2002](#)). The 2:1 resonance is regarded to result in enhanced tidal dissipation which forms spiral arms, giving early superhumps with almost the same period as the orbital period, and will be triggered at $\sim 0.61a$ in XTE J1859+226. WZ Sge-type dwarf novae also show characteristic reflare ([Kato 2015](#)), as seen also in XTE J1859+226 ([Zurita et al. 2002](#)). In our data, the estimated disc radius $\sim 0.67a$ on T1 exceeds the 2:1 resonance radius and it seems to shrink under the 3:1 resonance radius at the latter stage of the outburst (see also Figures 1 & 2 in [Ichikawa et al. \(1993\)](#) for reference). The overall X-ray and optical light curves of the outburst in XTE J1859+226 are similar to those in WZ Sge-type stars (e.g., [Neustroev et al. 2018](#)), and this would also support our idea.

7.3 Irregular Disc Geometry at the Late Outburst

On T4 and T5, we do not obtain reasonable fits, and the observations are inconsistent with the calculations in Sec. 7.1.2 showing that irradiation will be quite weak in the late stage of the outburst in comparison with that in the early stage. Although it is difficult to evaluate the irradiation degree with our current SED fits accurately, it is related to confirm if X-ray irradiation makes optical slow decline. Considering that other emission mechanisms are unlikely as discussed in Sec. 7.1.2, we suggest that the assumptions in our model are not applicable for T4 and T5, i.e., irregular outer disc geometry possibly producing non-steady state would be formed in this outburst. Our interpretation of the time-evolved disc geometry is displayed in Figure 9. Such anomalous geometry at the late outburst may be induced by cooling wave propagating from the outer disc to the inner disc at the final stage of the exponential decline as expected in numerical simulations including irradiation effect ([Dubus et al. 2001](#)). Its propagation quenches an outburst while altering the surface density profile. However, the predicted temperature distribution which drops drastically at the outer disc at the late outburst does not meet our observations showing the high temperature of the outer disc on T4 and T5. Therefore another mechanism would be required as the origin of irregular geometry.

We firstly consider the effect by thermal-tidal instability. As described in the previous subsection, the orbital parameters of XTE J1859+226 mean that the dissipation of the angular momentum on the outer edge of the disc can be enhanced by the tidal forces worked by the secondary ([Whitehurst 1988](#)). The thermal-tidal instability naturally explains the slow decline of optical light curves without irradiation by the mass at the outer disc piled via the enhanced tidal forces ([Osaki 1989](#)). Then, the outer disc is expected to become thicker than the standard disc, and the response for the X-ray illumination will change from the standard one. The piled mass keeps the outburst state at the outer disc, and a high-temperature outer disc will be reproduced simultaneously. Actually, the existing model including not irradiation but the thermal-tidal instability ([Ichikawa et al. 1994](#)) shows that the outer disc has a complex temperature dependence (see Figures 3 & 5 in that paper), and that is hotter than the standard temperature distribution expected from the inner steady state. However, this kind of temperature dependence would not completely meet the fact that the hard UV spectral shape is best produced in the right panels of Figure 6 and Figure 7 on T4 and T5, since these SEDs mean not complicated geometry but that the outer disc has a standard temperature distribution given by $T(R) \propto R^{-3/4}$ with higher normalisation than the inner disc. Next we consider that a wind launched from the outer disc on T1–3 by irradiation. The wind may be the origin of irregular geometry, since it can make non-steady outer disc with viscous timescales by altering net accretion rate from that expected from the steady state. Except these two, as [Hynes et al. \(2002\)](#) suggested, there may be a possibility that the disc become warped by irradiation and that irradiation behaviour at the outer surface changes ([Wijers & Pringle 1999](#); [Ogilvie & Dubus 2001](#)); however, it seems unlikely because this kind of instability is effective only in long-period (more than 1 day) systems.

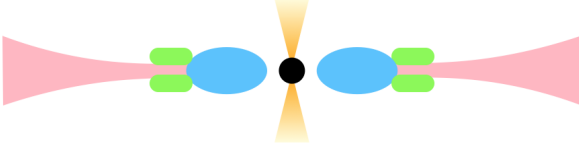
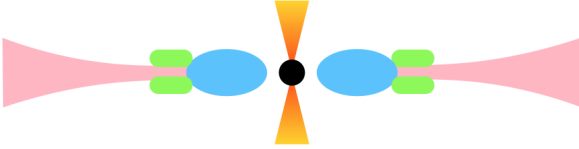
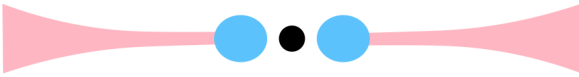
T1: very high state (truncated disc + standard irradiation)**T2: very high state (truncated disc + standard irradiation)****T3: bright high/soft state (extended disc + standard irradiation)****T4: dim high/soft state (extended disc + anomalous irradiation)****T5: soft-to-hard transition (growing hot flow + anomalous irradiation)**

Figure 9. Schematic picture of time-evolved accretion geometry in the 1999–2000 outburst of XTE J1859+226. The black circle is a black hole. The pink, blue, green, and orange structures represent an accretion disc, an optically-thin hot flow, a low-temperature optically-thick Comptonization component, and jet ejection, respectively.

These possibilities raised above may be testable with fast photometric data simultaneous with X-ray observations. If the model in Ichikawa et al. (1994) is correct, the optical/UV emission is dominated by intrinsic luminosity of the underlying disc at the outer region, and hence, it will vary only very slowly, and non-correlated optical variability inherent to the outer disc may be observable. On the contrary, if the emission is dominated by reprocessing, the optical/UV variations will significantly correlate with the X-ray fast variations. If the warp precessions are dominant, strong optical periodicity as well as fast optical variability from reprocessing would be observed. Also, numerical simulations including irradiation and thermal-tidal instability will be necessary to reproduce the irregular height distribution. This kind of simulations could solve the mismatch between the simula-

tions by Ichikawa et al. (1994) and our observations, which is described in the preceding paragraph.

8 CONCLUSIONS

We analyzed the 5 sets of broadband spectra from XTE J1859+226 during its 1999–2000 outburst by using the best current model of the irradiated disc continuum with the expected irradiation dominated $H \propto R^{9/7}$ shape, giving $T(R) \propto R^{-3/14}$. This works extremely well in the bright stages of the outburst, and is able to fit the X-ray, UV and optical continua spectra, though the IR requires a small contribution from the jet whose power tracks the hard X-ray continuum. The solid angle subtended by the irradiated outer disc is observed to decrease by $\sim 25\%$ as the source flux drops by a factor 2, and the spectrum softens from the very high state to the disc dominated high soft state. The changing solid angle implied our fits are exactly consistent with the predictions of scale height of the irradiated outer disc and scattering in a thermal wind at the early stage of the outburst, with an albedo of ~ 0.9 , as expected for such strongly ionised material (see e.g., Done et al. 2018) and as inferred for other LMXBs (de Jong et al. 1996).

The last two spectra, which are much lower in X-ray flux, are not well explained by these models. The optical and UV spectra have a different shape than predicted by the standard illuminated disc. Although it is difficult to evaluate the irradiation degree in these spectra, the lower inner disc luminosity and temperature mean that the scale height of the outer disc is smaller and that the thermal scattering wind is much less effective. This instead predicts a substantially smaller solid angle for the illumination than in the brighter spectra taken earlier in the outburst. These late spectra are better fitted by the unilluminated standard disc, which has $T \propto R^{-3/4}$. However, the models without illumination have an implied mass accretion rate through the outer disc, which is much higher than that which powers the inner disc. Therefore we suggest irregular outer disc geometry possibly producing non-steady flow developed at the late outburst.

Our analyses also imply that the outer disc shrinks by more than a factor of 2. Such large shrinkage of the disc can be triggered by enhanced dissipation due to the thermal-tidal instability. Since this system likely has an extremely small mass ratio, this kind of instability should work. The only calculation so far of the thermal-tidal instability in LMXBs does not include illumination, but the temperature distribution towards the end of the outburst is clearly far from steady state. It is, however, unclear if the thermal-tidal instability can be the origin of irregular outer disc geometry expected from our results, and a wind launched by irradiation at the early outburst may be also possible as the origin. Better models including irradiation in the bright phases of the outburst may be able to match the observed behaviour, while better data – specifically including high time resolution UV photometry such as UVSat (Pigulski et al. 2017) – should determine whether the UV flux is due to X-ray irradiation or intrinsic heating of the outer disc.

ACKNOWLEDGEMENTS

This work was financially supported by the Grant-in-Aid for JSPS Fellows for young researchers (M. Kimura). C. Done acknowledges the Science and Technology Facilities Council (STFC) through grant ST/P000541/1 for support.

REFERENCES

- Allen C. W., 1973, *Astrophysical quantities*
- Begelman M. C., McKee C. F., 1983, *ApJ*, **271**, 89
- Begelman M. C., McKee C. F., Shields G. A., 1983, *ApJ*, **271**, 70
- Brocksopp C., et al., 2002, *MNRAS*, **331**, 765
- Cardelli J. A., Clayton G. C., Mathis J. S., 1989, *ApJ*, **345**, 245
- Casella P., Belloni T., Homan J., Stella L., 2004, *A&A*, **426**, 587
- Chen W., Shrader C. R., Livio M., 1997, *ApJ*, **491**, 312
- Coriat M., Fender R. P., Dubus G., 2012, *MNRAS*, **424**, 1991
- Corral-Santana J. M., Casares J., Shahbaz T., Zurita C., Martínez-Pais I. G., Rodríguez-Gil P., 2011, *MNRAS*, **413**, L15
- Cunningham C., 1976, *ApJ*, **208**, 534
- Czerny B., Elvis M., 1987, *ApJ*, **321**, 305
- Davis S. W., Hubeny I., 2006, *ApJS*, **164**, 530
- Done C., Gierliński M., Kubota A., 2007, *A&ARv*, **15**, 1
- Done C., Davis S. W., Jin C., Blaes O., Ward M., 2012, *MNRAS*, **420**, 1848
- Done C., Tomaru R., Takahashi T., 2018, *MNRAS*, **473**, 838
- Dubus G., Lasota J.-P., Hameury J.-M., Charles P., 1999, *MNRAS*, **303**, 139
- Dubus G., Hameury J.-M., Lasota J.-P., 2001, *A&A*, **373**, 251
- Dunn R. J. H., Fender R. P., Körding E. G., Belloni T., Cabanac C., 2010, *MNRAS*, **403**, 61
- Farinelli R., et al., 2013, *MNRAS*, **428**, 3295
- Fender R. P., Belloni T. M., Gallo E., 2004, *MNRAS*, **355**, 1105
- Fitzpatrick E. L., 1999, *PASP*, **111**, 63
- Fitzpatrick E. L., Massa D., 2007, *ApJ*, **663**, 320
- Gandhi P., et al., 2011, *ApJ*, **740**, L13
- Gierliński M., Done C., Page K., 2009, *MNRAS*, **392**, 1106
- Higinbottom N., Proga D., 2015, *ApJ*, **807**, 107
- Hynes R. I., 2005, *ApJ*, **623**, 1026
- Hynes R. I., Haswell C. A., Chaty S., Shrader C. R., Cui W., 2002, *MNRAS*, **331**, 169
- Ichikawa S., Hirose M., Osaki Y., 1993, *PASJ*, **45**, 243
- Ichikawa S., Mineshige S., Kato T., 1994, *ApJ*, **435**, 748
- Jimenez-Garate M. A., Raymond J. C., Liedahl D. A., 2002, *ApJ*, **581**, 1297
- Kato T., 2015, *PASJ*, **67**, 108
- Kato T., Mineshige S., Hirata R., 1995, *PASJ*, **47**, 31
- King A. R., 1998, *MNRAS*, **296**, L42
- King A. R., Ritter H., 1998, *MNRAS*, **293**, 42P
- Krolik J. H., Kallman T. R., 1982, in *Bulletin of the American Astronomical Society*. p. 955
- Kubota A., Done C., 2004, *MNRAS*, **353**, 980
- Kubota A., Makishima K., Ebisawa K., 2001, *ApJ*, **560**, L147
- Lasota J.-P., 2001, *New Astron. Rev.*, **45**, 449
- Maccarone T. J., 2003, *A&A*, **409**, 697
- Merloni A., Di Matteo T., Fabian A. C., 2000, *MNRAS*, **318**, L15
- Mineshige S., Wheeler J. C., 1989, *ApJ*, **343**, 241
- Nandi A., et al., 2018, *Ap&SS*, **363**, 90
- Narayan R., Yi I., 1995, *ApJ*, **452**, 710
- Neustroev V. V., et al., 2018, *A&A*, **611**, A13
- Ogilvie G. I., Dubus G., 2001, *MNRAS*, **320**, 485
- Osaki Y., 1989, *PASJ*, **41**, 1005
- Osaki Y., 1996, *PASP*, **108**, 39
- Osaki Y., Meyer F., 2002, *A&A*, **383**, 574
- Pei S., Ding G., Li Z., Lei Y., Yuen R., Qu J., 2017, *Ap&SS*, **362**, 118
- Pigulski A., et al., 2017, in *Second BRITE-Constellation Science Conference: Small satellites, big science*, Proceedings of the Polish Astronomical Society volume 5, held 22-26 August, 2016 in Innsbruck, Austria. Other: Polish Astronomical Society, Bartycka 18, 00-716 Warsaw, Poland, pp.76-81. pp 76–81 ([arXiv:1711.10366](https://arxiv.org/abs/1711.10366))
- Remillard R. A., McClintock J. E., 2006, *ARA&A*, **44**, 49
- Seaton M. J., 1979, *MNRAS*, **187**, 73P
- Shakura N. I., Sunyaev R. A., 1973, *A&A*, **24**, 337
- Shidatsu M., Done C., Ueda Y., 2016, *ApJ*, **823**, 159
- Shimura T., Takahara F., 1995, *ApJ*, **445**, 780
- Sriram K., Rao A. R., Choi C. S., 2013, *ApJ*, **775**, 28
- Sutton A. D., Done C., Roberts T. P., 2014, *MNRAS*, **444**, 2415
- Tanaka Y., Shibazaki N., 1996, *ARA&A*, **34**, 607
- Tetarenko B. E., Sivakoff G. R., Heinke C. O., Gladstone J. C., 2016, *ApJS*, **222**, 15
- Tetarenko B., Dubus G., Lasota J.-P., Heinke C., Sivakoff G., 2018, *MNRAS*, **480**, 2
- Uemura M., Kato T., Pavlenko E., Shugarov S., Mitskevich M., Fried R. E., Sano Y., 2004, *PASJ*, **56**, S147
- Veledina A., Poutanen J., Vurm I., 2011, *ApJ*, **737**, L17
- Whitehurst R., 1988, *MNRAS*, **232**, 35
- Wijers R. A. M. J., Pringle J. E., 1999, *MNRAS*, **308**, 207
- Woods D. T., Klein R. I., Castor J. I., McKee C. F., Bell J. B., 1996, *ApJ*, **461**, 767
- Zdziarski A. A., Skinner G. K., Pooley G. G., Lubiński P., 2011, *MNRAS*, **416**, 1324
- Zurita C., et al., 2002, *MNRAS*, **334**, 999
- Życki P. T., Done C., Smith D. A., 2001, *MNRAS*, **326**, 1367
- de Jong J. A., van Paradijs J., Augusteijn T., 1996, *A&A*, **314**, 484
- van Paradijs J., McClintock J. E., 1994, *A&A*, **290**, 133

This paper has been typeset from a $\text{\TeX}/\text{\LaTeX}$ file prepared by the author.